

to appear in ApJ, September 1999

The Surface Density of Extremely Red Objects

D. Thompson¹, S. V. W. Beckwith², R. Fockenbrock, J. Fried,
H. Hippelein, J.-S. Huang, B. von Kuhlmann, Ch. Leinert,
K. Meisenheimer, S. Phleps, H.-J. Röser, E. Thommes³, C. Wolf

Max-Planck-Institut für Astronomie,

Königstuhl 17, D-69117 Heidelberg, Germany

Electronic mail: djt,svwb,fock,fried,hippelei,huang,kuhlmann,leinert,
meise,phleps,roeser,thommes,cwolf@mpia-hd.mpg.de

ABSTRACT

We present initial results from a field survey for extremely red objects (EROs, defined here as $(R-K') \geq 6^m$) covering 154 square arcminutes of sky, from the first of 7 deep, wide-field K' images obtained as part of the Calar Alto Deep Imaging Survey (CADIS). The 5σ point source detection limits are $K' = 20^m5$ and $R = 25^m0$, while extended-source limits are up to 0^m50 – 0^m75 brighter. We identify a total of 8 bright EROs with $K' \leq 19^m0$. Six of these bright EROs are resolved and are likely to be galaxies, while the remaining 2 are unresolved, with colors consistent with their being low-mass Galactic stars. We derive a surface density for the 6 bright, extragalactic EROs of 0.039 ± 0.016 arcmin⁻², higher by a factor of 4 than previous values. We estimate that the volume density of bright EROs to be as high as that of nearby Seyfert galaxies.

Subject headings: cosmology: observations — early universe — galaxies: formation — infrared: galaxies

¹Current address: MS 320-47 Caltech, Pasadena, CA 91125, USA. Email: djt@mop.caltech.edu

²Current address: STScI, 3700 San Martin Dr., Baltimore, Md. 21218 USA. Email: svwb@stsci.edu

³Current address: Royal Observatory, Blackford Hill, Edinburgh, EH9 3HJ, UK. Email: emt@roe.ac.uk

1. Introduction

Significant numbers of massive galaxies have been identified in the near-infrared with colors so red that they are not found in surveys that select galaxies at visual wavelengths. Such objects have been named *extremely red objects* (EROs). With surface densities similar to that of bright quasars (Hu & Ridgeway, 1994), they represent an important component of the population of high-redshift galaxies.

The identification of EROs coincided with the development and implementation of infrared arrays for astronomical research, the first EROs being noted in the K-band surveys of Elston, Rieke, & Rieke (1988, 1989). Since then, many groups have identified objects with extremely red colors (McCarthy, Persson, & West 1992; Eisenhardt & Dickinson 1992; Persson et al. 1993, Hu & Ridgeway 1994, Soifer et al. 1994, Dey, Spinrad & Dickinson 1995, Djorgovski, et al. 1995, among others), though often with widely different definitions of *extremely red*. These objects were primarily identified in the fields around high-redshift active galactic nuclei, i.e. around radio galaxies and quasars. In this paper, we define the selection criteria for bright EROs to be $K' \leq 19^m0$ and with $(R-K') \geq 6^m$.

The broad-band spectral energy distributions (SEDs) of these galaxies were initially thought to be fitted best by an old stellar population, such as found in present-day elliptical galaxies. In this scenario, a redshifted ($z > 0.85$) strong 4000Å-break falling between the R and K filter bandpasses and the lack of any appreciable restframe UV light from a young population of stars are responsible for the extremely red colors. An alternative interpretation is that these galaxies are starbursts or active galactic nuclei (AGN), perhaps triggered by a merging event. In this scenario, the presence of significant quantities of interstellar dust hides the star-forming regions or AGN, considerably reddening the observed SEDs. These would also lie at redshifts $1 < z < 2$, which shifts the restframe UV into the optical bandpass while still sampling the restframe optical/near-IR wavelengths in the K filter.

Archetypal examples of each of these interpretations have been identified. LBDS 53W091 (Dunlop et al. 1996) is a faint radio galaxy at a redshift of 1.55, derived from an absorption line spectrum obtained at restframe UV wavelengths. Spectral modeling suggests an elliptical galaxy spectrum with an age of up to 3.5 Gyr (Dunlop et al. 1996, Spinrad et al. 1997, but see Bruzual & Magris 1997 for an alternative viewpoint), implying a much higher redshift of formation for this system. In contrast, HR10 (Hu & Ridgeway 1994) has been identified as a dusty starforming galaxy, perhaps with an active nucleus, at $z = 1.44$ (Graham & Dey 1996). Detections of this galaxy at submillimeter and millimeter wavelengths support the interpretation that the SED is dominated by the presence of dust (Cimatti et al. 1998).

In both cases, the EROs are most likely to lie in the redshift range $1 < z < 2$. It is difficult to produce such red colors at lower redshifts, while higher redshift objects become exceedingly luminous. If EROs are dominated by old stellar populations, then massive galaxy formation was well underway at $z > 3$. Dust-dominated EROs, however, imply that much of the massive galaxy

formation could actually occur at late times, supporting hierarchical galaxy formation models. The contrasting implications these two scenarios have for the history of galaxy formation is the primary driver behind continuing work on these objects.

We have therefore started a wide-area field survey to select an unbiased and statistically significant sample of EROs for further study. This paper presents initial results from the first of seven fields, obtained as part of the Calar Alto Deep Imaging Survey (CADIS, Meisenheimer et al. 1997), each of which will cover ~ 160 square arcminutes. Section 2 describes the observations and reductions. Section 3 includes a discussion of the sample selection, morphology, and surface and volume density of the EROs identified here. Section 4 gives a brief summary of this paper.

2. Observations and Reductions

The field observed in this paper is centered on $\alpha_{1950} = 16^h 23^m 29^s$ $\delta_{1950} = +55^\circ 50' 47''$ (hereafter the 16 h field). It is one of 7 fields in the CADIS survey (Meisenheimer et al. 1997), chosen to be free of bright stars or galaxies, known galaxy clusters, and in regions of minimal extinction due to Galactic cirrus. All magnitudes quoted in this paper are referred to α Lyra.

2.1. K' imaging

The K' imaging was obtained with the Omega-Prime camera (Bizenberger et al. 1998) at the prime focus of the Calar Alto 3.5m telescope on UT 1996 June 7-8 and UT 1996 August 22-29. The majority of these nights were photometric. Omega-Prime is a direct imaging camera equipped with a HAWAII 1024² HgCdTe array. The image scale is 0.396"/pixel (6.75 arcminute square field of view). Data were taken in a 2 \times 2 mosaic to cover as much of the CADIS survey field (16' diameter) as possible. The K' filter ($\lambda_{\text{cent}} = 2.12 \mu\text{m}$, $\Delta\lambda = 0.35 \mu\text{m}$, see Wainscoat and Cowie 1991) was used because its bluer bandpass relative to a standard K filter significantly reduces the thermal background seen by the array.

The data were reduced with a standard infrared reduction algorithm in IRAF⁴. A sky frame was constructed from 6 to 12 temporally adjacent images, scaled to have the same median counts before averaging all but the 1 or 2 most extreme values in each pixel, effectively removing stars from the final sky image. The sky frame was then scaled to and subtracted from the data frame and the result divided by a normalized dome flat to remove pixel-to-pixel fluctuations in quantum efficiency.

On photometric nights, standard stars from the UKIRT faint standards list (Casali &

⁴IRAF is distributed by the National Optical Astronomy Observatories, which are operated by the Association of Universities for Research in Astronomy, Inc., under cooperative agreement with the National Science Foundation.

Hawarden 1992) were observed every 2-3 hours at several different airmasses to determine both a photometric zero point and an extinction correction. Individual images were then corrected for extinction and put onto a common photometric scale. Night to night variations of the zero points were under 0.1 magnitude, giving a measure of the systematic uncertainty in the K' calibrations.

As IRAF was not able to handle either the large number of frames (1209) or the large size of the data set (4.8 GB), a procedure for IDL was developed to stack the individual images into the final mosaic. Known bad pixels were ignored and only good pixels were included in the mosaic. The software used a multi-pass sigma-clipping algorithm to reject cosmic rays and other transient phenomena (e.g meteors and satellites).

The final mosaic is 2419×2546 pixels ($15'.96 \times 16'.80$), including regions of higher noise around the edge where coverage was incomplete. The deepest portion of the mosaic, with per pixel exposure times greater than 6000 seconds, covers the central ~ 12.5 arcmin square with a seeing of 1.1 arcsec full-width at half-maximum (FWHM). A grayscale image of the exposure time map, along with the relative fields of view for the optical and infrared data, is shown in Figure 1. The central portion of the K' mosaic has a 5σ point source detection limit of $K' = 20^m5$, within an aperture diameter of $2''.2$, twice the seeing FWHM. Limits for extended sources are up to 0^m50 – 0^m75 brighter, depending on the object morphology.

2.2. R -band imaging

The R -band imaging was obtained with the CAFOS reimaging camera at the Calar Alto 2.2 m telescope on UT 1996 May 15 (5×500 s, $1''.3$ seeing) and UT 1997 February 5 (4×700 s $1''.6$ seeing). CAFOS was equipped with a LORAL 2048² CCD ($0.33''/15 \mu\text{m}$ pixel) for the May observations, and with a SITe 2048² CCD ($0.53''/24 \mu\text{m}$ pixel covering a circular field of view ~ 16 arcminutes in diameter) for the remaining observations. The R filter used in CADIS ($\lambda_{\text{cent}} = 648$ nm, $\Delta\lambda = 171$ nm) is slightly narrower and bluer than a standard Johnson R filter. This difference has no significant impact on the goals of this survey.

The data were reduced with the MIDAS software package. Following bias subtraction and flatfielding, multiple exposures obtained on a single night were shifted into coincidence, bad pixels and cosmic rays masked out, then summed to form a deep image for that night.

Flux calibration of the R -band data was established relative to two stars in the 16 h field for which we have good spectrophotometry. These stars were calibrated against an HST UV spectrophotometric standard (AGK+81°266) as well as 3 stars from Oke (1990). The magnitudes of the two 16 h field reference stars in the R filter were determined by integrating their calibrated spectra over the R filter bandpass and instrumental transmission curve. The 2σ limits were established within an aperture diameter twice the seeing FWHM, scaling from the per-pixel noise in the stacked data. A full description of the calibration of the CADIS optical data set can be found in Fockenbrock (1998).

2.3. Object Detection

Objects were separately identified on the deep R and K' images using the Source Extractor software (Bertin & Arnouts 1996) and the resulting lists merged into a master catalog. This catalog was then used to extract photometric magnitudes for all objects in each individual exposure (mosaics from each night for the K' data) using photometry software (Meisenheimer & Röser 1986) incorporating a Gaussian weighting function, designed to compensate for variations in seeing between individual exposures. The procedure recovers accurate *colors* for all objects, but underestimates the total magnitude for extended objects. For the faint galaxy images from which the sample of EROs was drawn, typically subtending only $1\text{--}2''$, the underestimate is of order 0.1 magnitude.

A final list of objects was selected from the master catalog, containing objects with K' magnitudes above the 5σ limit of 20^m5 that also appear on at least one of the two R images (from the LORAL and SITe CCDs). Figure 1 shows a contour map and image of the exposure time, overlaid with the outline of the survey area. The full area imaged in both K' and R covers 154 square arcminutes.

3. Discussion

3.1. ERO Selection

We select objects with extremely red colors from the color-magnitude diagram for the full survey area, shown in Figure 2. We define the selection criteria for bright EROs as objects with $K' \leq 19^m0$ and $(R-K') \geq 6^m$. A more detailed plot of this region of the color-magnitude diagram is shown in Figure 3. Eight objects in our survey field meet these selection criteria. Their positions, magnitudes and colors are summarized in Table 1, while finding charts from the K' data are given in Figure 4.

The magnitude limit defining the bright sample of EROs is partially driven by the current data: most EROs brighter than $K' \leq 19^m0$ are detected above the 2σ limit in R while most of those fainter than this are not. This also represents the practical limit for obtaining followup near-infrared spectroscopy at 8m-class telescopes (Moorwood & Spyromilio 1997) with exposure times of order 1 hour.

In the absence of significant dust extinction, the reddest galaxy colors will come from the oldest stellar populations at any redshift. A present-day elliptical galaxy SED under a no-evolution model peaks in color at $1 \lesssim z \lesssim 3$ (ignoring the Lyman break at higher redshift), with an $R-K'$ color of about 6. For an old stellar population, this color is produced by a combination of the cosmological k-corrections and a strong 4000\AA -break lying between the two bandpasses. Since all galaxies should be bluer than this limit, selecting objects with $R-K' \geq 6^m$ will isolate a sample of galaxies with extremely red colors. The specific choice of $R-K' \geq 6^m0$ is, however, also

motivated by historical precedence, approximating the limits used to identify other EROs in the literature. Such objects were identified as lying away from the locus of other field objects in the color-magnitude diagram. However, the areas surveyed, and thus the number of objects detected, were generally too small to address this point statistically.

Figure 5 displays histograms of the $R-K'$ colors for objects with $16^m \leq K' \leq 20^m$ in 1^m bins. Table 2 lists the mean color and FWHM for the Gaussian least-square fits which are also plotted in Figure 5. For example, in the range $18^m5 \leq K' \leq 19^m5$, the bin containing most of the EROs, the mean color is 3^m92 and the standard deviation is 1^m11 . An $(R-K') \geq 6^m$ selection criterion therefore corresponds to colors that deviate by more than about two standard deviations from the mean color. The extremely red galaxies selected here are thus the reddest 2% of the population and should consist of the oldest and/or the dustiest high redshift galaxies.

There is a distinct trend to redder colors at fainter magnitudes, with the mean $(R-K')$ color becoming 0^m7 redder between $K' = 16^m5$ and $K' = 19^m5$. This continues the trend noted at brighter magnitudes in (I-K) colors by Huang et al. (1997). Over the range sampled by our data, this trend probably reflects an increasing fraction of high redshift galaxies.

There are an additional 43 objects with $(R-K') \geq 6^m$ in the range $19^m0 < K' \leq 20^m0$. These fainter EROs lie only in the central 120 square arcminutes of the survey field, where the overlap of the two sets of R -band data reach deep enough to select EROs with $K' \leq 20^m0$. We note that since both the color and color dispersion for the objects in the 16^h field increase with increasing magnitudes, the EROs in this fainter magnitude range may no longer have truly extreme colors. The current optical data do not have sufficient depth to address this more quantitatively.

We chose to set the detection limit in the R data at 2σ to ensure that all of the EROs are selected, at the expense of some possible contamination of the sample. In practice, contamination is likely to be low. Consider a Malmquist bias vector defined on the color-magnitude diagram (Figure 3). For objects near the ERO selection region, it would be dominated by the uncertainties in the R -band magnitudes, since most of the objects there are well-detected at K' but near the 2σ detection limit in R . The Malmquist bias vector would thus point to *bluer* colors and slightly brighter K' magnitudes. Inspection of Figure 3 shows that there are a comparable number of objects which could scatter into the ERO region as are already there, so contamination of the sample is likely to be low and would be coming from objects with redder colors.

3.2. Morphology and Environment

The radial brightness profiles of the EROs were compared to those of several stars near each object to determine whether the EROs are resolved. Five of the 8 bright EROs are easily resolved, with FWHMs ranging from $1''.4$ to $2''.3$ in $1''.1$ seeing, and are therefore likely to be galaxies. Subtracting the intrinsic seeing in quadrature gives deconvolved FWHMs ranging from $0''.9$ to $2''.0$. Such sizes are similar to both HR10 ($0''.7$, Hu & Ridgeway 1994) and 53W091 ($1''.3$, Dunlop et al.

1996). A sixth object, C16-ERO3, is formally resolved, but at a low statistical significance, with a deconvolved FWHM $\leq 0''.4$.

The remaining 2 bright EROs in the 16 h field are unresolved. Their broadband colors indicate that they are low mass Galactic stars. One has subsequently been spectroscopically confirmed as a low mass star of spectral type L1 (Wolf et al. 1998). The second is well-detected in the CADIS filters ($K' = 16^m32$), with colors fully consistent with a star of spectral type M9 (Wolf et al. 1998), though without spectroscopic confirmation we cannot completely rule out that the object may be a compact galaxy or AGN at high redshift. Finding charts for these two objects can be found in Wolf et al. (1998), and they are not considered further in this paper.

Only one of the six resolved EROs is significantly non-circular (C16-ERO1). The deconvolved FWHMs along the major and minor axes are $1''.9$ and $1''.1$, respectively, with the major axis oriented at a position angle (PA) of 143° , east of north. There is also a companion ERO with $K' > 19^m0$, $2''.8$ away at PA = 126° . The proximity of the second ERO and the apparent alignment between the PA of C16-ERO1 and the direction to the fainter galaxy suggest that this might be an interacting system. C16-ERO1 and C16-ERO2 also make the closest pair of EROs in the current sample, separated by $39''.2$ at PA = $125^\circ.5$, possibly indicating the presence of a cluster or group. One other object (C16-ERO4) has a fainter ERO companion nearby ($4''.9$ away at PA = 127°), though there is no evidence for interaction in the current data set.

Of the fainter 43 EROs, 37 are either clearly or marginally resolved. Below $K' \sim 19^m5$, it becomes difficult to distinguish between unresolved and slightly extended sources on the survey data. Nevertheless, the fainter EROs in this field are clearly dominated by galaxies.

3.3. Surface Density

The 6 bright, extragalactic EROs identified here were found in an area of 154 arcmin^2 , yielding a surface density of $0.039 \pm 0.016 \text{ arcmin}^{-2}$ (poisson uncertainties). This density is a factor of four higher than found by Hu & Ridgeway (1994), estimated from 100 arcmin^2 of I and K' data from the Hawaii Deep K-band Surveys (Cowie et al. 1994). In their survey, Hu & Ridgeway found no galaxies as red as HR10, implying a surface density of $\lesssim 0.01 \text{ arcmin}^{-2}$. The difference is not statistically significant due to the currently large uncertainties from the small number statistics as well as a possible contribution from field-to-field variations. Combining these data with those from future fields obtained as part of this survey will reduce this uncertainty to $\sim 15\%$. Still, the surface density of EROs is comparable to or higher than that of bright ($B < 22^m$) quasars, making the EROs a significant population.

Dey, Spinrad, and Dickinson (1995) suggest that EROs are more common along the line of sight to or clustered with high redshift radio galaxies and quasars. Estimates of the surface density range up to 10-100 times that of the field EROs. If the EROs are at the same redshifts as the high-redshift AGN, then many of them would have luminosities significantly in excess of L^* .

With the EROs in the foreground there is the possibility of a magnification bias, where the ERO (or a group or cluster containing it) is acting as a gravitational lens for the background AGN. This higher surface density in the fields of high-redshift AGN may also reflect what we term an “observational bias.” This is a combination of (i) AGN were a common target for observations in the near-IR, (ii) unusual objects of any sort were noted (here objects with extremely red colors) when the data were published, and (iii) earlier generations of near-IR imagers had fields of $\sim 1 \text{ arcmin}^2$. A systematic measurement of the surface density in AGN fields still remains to be done.

Guiderdoni et al. (1997, their model C) predict the surface density ($\sim 0.05 \text{ arcmin}^{-2}$) of high-redshift dusty star-forming galaxies observed at far-infrared wavelengths that is remarkably similar to the surface density of bright EROs found here, suggesting that EROs may be dusty starbursts. The predictions were based on local ultra-luminous infrared galaxies, actively forming stars but completely shrouded by dust. The detection of significant quantities of dust in HR 10 (Cimatti et al. 1998) supports this picture.

Including the additional 43 EROs with $K' \leq 20^m$, the surface density is $0.33 \pm 0.05 \text{ arcmin}^{-2}$. As noted above, the fainter sample is not well defined over the survey area, and this is only an estimate to the true surface density of faint EROs. The depth of the R band data is currently the limiting factor, and deeper imaging will allow us to make a stronger statement about these fainter EROs.

3.4. Volume Density

We can derive a volume density of EROs if we can estimate the redshift range over which they occur. This volume density would then be directly comparable to known populations of galaxies, perhaps providing some insight into their nature.

If the ERO population is dominated by old (elliptical) galaxies, the red color would be coming from a strong 4000\AA break. This spectral break comes primarily from Balmer continuum limit and Ca H+K absorption lines and can significantly redden an ($R-K'$) color when the break lies between the two filter bandpasses. For the R filter used here, this implies a redshift beyond $z = 0.85$.

If, on the other hand, the ERO population is dominated by dusty starburst galaxies, the red color would be due to dust extinction reddening a flat SED. A color of ($R-K'$) $\sim 6^m$ can be produced at $z = 0.85$ by a V-band extinction of $A_V \sim 5^m$, assuming the Seaton (1979) Milky Way extinction law. In the grayer extinction law of Calzetti et al. (1994), derived empirically from a sample of local starburst galaxies, a factor of two more extinction would be required to give similar results. The steeply rising extinction curves at shorter wavelengths, however, imply that less dust extinction would be required to produce the same reddening at higher redshifts. In practice, a moderate continuum decrement across the 4000\AA break is also seen in relatively young

stellar populations, contributing to the red color and relaxing the extinction requirements. We therefore adopt a redshift of $z = 0.85$ as the lower redshift limit for both types of galaxies.

For the high redshift limit, consider an L^* galaxy at $z = 2$. It would have an apparent magnitude of $K' \simeq 20^m3$ ($H_0 = 70 \text{ km s}^{-1} \text{ Mpc}^{-1}$ and $q_0 = 0.1$), assuming only passive evolution (evolution and k-corrections from Poggianti 1997 and Fioc & Rocca-Volmerange 1997 give similar results). Our selection of bright EROs at $K' \leq 19^m$ is thus already sampling the luminosity function well above L^* at $z = 2$. Beyond this redshift, the galaxies would have to be intrinsically as luminous as bright quasars to be selected as EROs. We therefore adopt the range $z \in [0.85, 2.0]$ where EROs are most likely to be found with the selection criteria used here.

The comoving volume covered in this redshift range over our survey field in the assumed cosmology is $3.55 \times 10^5 \text{ Mpc}^3$. For the six bright EROs in our sample, this yields a volume density of $1.7 \pm 0.7 \times 10^{-5} \text{ Mpc}^{-3}$. Extending the redshift range down to $z = 0.5$ would only increase the comoving volume by 15%. Increasing the upper redshift limit to $z = 3$ would approximately double the sampled volume. The volume density derived here is, therefore, not very sensitive to the assumed redshift range.

We can compare this estimate of the volume density of EROs with that of other known types of objects. For quasars ($M_{B \leq -23^m}$), the volume density in a similar redshift range (Boyle 1991) is only $2 \times 10^{-6} \text{ Mpc}^{-3}$, a factor of 8 lower than the bright ERO density. A simple extrapolation of the Boyle luminosity function to $M_B \sim -19^m$ (it is strictly only valid for $M_B \leq -21^m$) is required to reach space densities similar to those of the EROs. Thus the *bright* ERO galaxies appear to be considerably more numerous than quasars, and perhaps as common as Seyfert Is in the local universe. The EROs, however, have been compared to both old ellipticals and young dusty starbursts, and it is perhaps more interesting to compare them to these groups of objects.

The red galaxies from the Canada-France Redshift Survey (CFRS, Lilly et al. 1995) represent a population of objects which do not undergo significant evolution from $z \sim 1$ to the present, similar to what would be expected of the EROs if they are dominated by old elliptical galaxies. The integrated luminosity function for the CFRS red galaxies reaches a volume density comparable to the EROs at a luminosity of $\sim 4L^*$. Thus, if the ERO population is dominated by old elliptical galaxies, then the EROs are very massive and suggest that the most massive systems collapsed early in the history of the universe. Such galaxies at $z \sim 1.5$ could also mark the location of high redshift (forming?) clusters or groups of galaxies.

Luminous infrared galaxies are often powered by strong starbursts or AGN, but emit most of their bolometric luminosity at restframe far-infrared wavelengths due to the presence of significant quantities of dust. The ERO population could be high-redshift analogs to these luminous infrared galaxies if the EROs are dominated by objects like HR10. The integrated luminosity function for the luminous infrared galaxies (Soifer & Neugebauer 1991) reaches a volume density comparable to the EROs at a bolometric luminosity of a few $\times 10^{11} L_\odot$, corresponding to $\sim 10L^*$. Thus, if the ERO population is dominated by young, dusty starbursts similar to the luminous infrared

galaxies, then many massive galaxies were undergoing formative mergers at relatively late times.

4. Summary

We have surveyed an area of 154 sq. arcmin to a 5σ point-source limit of $K' = 20^m5$, representing the largest contiguous field imaged in the near infrared at this depth to date. From these data, we have selected 8 EROs with $K' \leq 19^m0$ and with $(R-K') \geq 6^m$.

Six of the 8 bright EROs are resolved at K' and are, therefore, most likely to be galaxies at high redshift ($z \geq 0.85$). These EROs have a surface density of 0.039 ± 0.016 arcmin $^{-2}$, or, with simple assumptions about their range of redshifts, a volume density comparable to that of Seyfert galaxies. Interpretations as to the nature of these galaxies range from old, evolved elliptical galaxies to young dusty starbursts or AGN.

The remaining 2 EROs are low-mass Galactic stars, either main sequence M stars or brown dwarfs (Wolf et al. 1998). Such low-mass stars can be seen to distances well beyond 100 pc, depending on their intrinsic luminosity. Morphological considerations alone rule out the possibility that the majority of the EROs with $K' \leq 20^m$ are low-mass stars. The true count of such stars in high-latitude fields will provide interesting constraints on Galactic structure and the faint end of the local stellar luminosity function.

EROs appear to be a significant population of galaxies absent from samples derived from observations at visual wavelengths. Future work on these objects will distinguish between the old elliptical and young dusty starburst interpretations. Observations at submillimeter (ground based) and mid- to far-infrared (SIRTF, NGST) wavelengths will be able to quantitatively determine how much dust, if any, is present. In either case, the EROs are likely drawn from a population of massive galaxies at high redshift. Whichever interpretation prevails, the EROs will provide important clues to the formation and evolution of massive galaxies.

We are grateful to the team that constructed the OMEGA camera, particularly M. McCaughrean and P. Bizenberger, without whom the wide field, deep K' survey would not have been possible. We also thank the staff at the Calar Alto observatory for support during the observing runs, and MPIA for support of the CADIS key project. This research was supported by the Max-Planck-Society.

REFERENCES

- Bertin, E. & Arnouts, S. 1996, *A&AS*, 117, 393.
- Bizenberger, P., McCaughrean, M., Thompson, D., & Birk, C., 1998, *SPIE Conference Proceedings*, vol. 3354, p. 825.
- Boyle, B. J. 1991, in *Texas/ESO-CERN Symposium on Relativistic Astrophysics, Cosmology, and Fundamental Physics*, eds. J. D. Barrow, L. Mestel, & P. A. Thomas, (N.Y.Acad.Sci.:New York), p. 14.
- Bruzual, G. A. & Magris, G. C. 1997, *IAU Symp.* 183.
- Calzetti, D., Kinney, A. L., & Storchi-Bergmann, T. 1994, *ApJ*, 429, 582.
- Casali, M. M. & Hawarden, T. 1992, *JCMT UKIRT Newsletter*, 4, 33.
- Cimatti, A., Andreani, P., Röttgering, H. & Tilanus, R. 1998, *Nature*, 392, 895.
- Cowie, L. L., Gardner, J. P., Hu, E. M., Songaila, A., Hodapp, K.-W., & Wainscoat, R. J. 1994, *ApJ*, 434, 114.
- Dey, A., Spinrad, H., & Dickinson, M. 1995, *ApJ*, 440, 515.
- Djorgovski, S., Soifer, B. T., Pahre, M. A., Larkin, J. E., Smith, J. D., Neugebauer, G., Smail, I., Matthews, K., Hogg, D. W., Blandford, R. D., Cohen, J., Harrison, W., & Nelson, J. 1995, *ApJ*, 438, L13.
- Dunlop, J., Peacock, J., Spinrad, H., Dey, A., Jimenez, R., Stern, D., & Windhorst, R. 1996, *Nature*, 381, 581.
- Eisenhardt, P. & Dickinson, M. 1992, *ApJ*, 399, L47.
- Elston, R., Rieke, G. H., & Rieke, M. J. 1989, *ApJ*, 341, 80.
- Elston, R., Rieke, M. J., & Rieke, G. H. 1988, *ApJ*, 331, L77.
- Fioc, M., & Rocca-Volmerange, B. 1997, *A&A*, 326, 950.
- Fockenbrock, R. 1998, Ph.D. Thesis, Ruprecht Karls Universität, Heidelberg, Germany.
- Graham, J. R. & Dey, A. 1996, *ApJ*, 471, 720.
- Guideroni, B., Bouchet, F. R., Puget, J.-L., Lagache, G. & Hivon, E. 1997, *Nature*, 390, 257.
- Hu, E. M. & Ridgeway, S. E. 1994, *AJ*, 107, 1303.
- Huang, J.-S., Cowie, L. L., Gardner, J. P., Hu, E. M., Songaila, A., & Wainscoat, R. J. 1997, *ApJ*, 476, 12.
- Lilly, S. J., Tresse, L., Hammer, F., Crampton, D., & Le Fevre, O. 1995, *ApJ*, 455, 108.
- McCarthy, P. J., Persson, S. E., & West, S. C. 1992, *ApJ*, 386, 52.
- Meisenheimer, K. & Röser, H.-J. 1986, in *The Optimization of the Use of CCD Detectors in Astronomy*, eds. J.-P. Baluteau & S. D’Odorico, (ESO:Garching), p. 227. (ESO-OHP:Garching bei München), p. 227.

- Meisenheimer, et al. 1997, in *The Early Universe with the VLT*, ed. J. Bergeron (Springer:Heidelberg), 165.
- Moorwood, A. F. M., & Spyromilio, J. 1997, in *The Early Universe with the VLT*, ed. J. Bergeron (Springer:Heidelberg), 21.
- Oke, J. B. 1990, *AJ*, 99, 1621.
- Persson, S. E., McCarthy, P. J., Dressler, A., Matthews, K. 1993, in *The Evolution of Galaxies and Their Environment*, ed. D. Hollenbeck et al., NASA Conference Publication #3190, p. 78.
- Poggianti, B. M. 1997, *A&ASupp. Ser.*, 122, 399.
- Seaton, M. J. 1979, *MNRAS*, 187, 73P.
- Soifer, B. T., Matthews, K., Djorgovski, S., Larkin, J., Graham, J. R., Harrison, W., Jernigan, G., Lin, S., Nelson, J., Neugebauer, G., Smith, G., Smith, J. D., & Ziomkowski, C. 1994, *ApJ*, 420, L1.
- Soifer, B. T., & Neugebauer, G. 1991, *AJ*, 101, 354.
- Spinrad, H., Dey, A., Stern, D., Dunlop, J., Peacock, J., Jimenez, R., & Windhorst, R. 1997, *ApJ*, 484, 581.
- Wainscoat, R. & Cowie, L. L. 1991, *AJ*, 103, 332.
- Wolf, C., Mundt, R., Thompson, D., Chaffee, Beckwith, S. V. W., F., Fockenbrock, Fried, J., R., Hippelein, H., Huang, J.-S., von Kuhlmann, B., Leinert, C., Meisenheimer, K., Phleps, S., Röser, H.-J., & Thommes, E. 1998, *A&A*, 338, 127.

Table 1. ERO properties

ID ^a	Position (J2000.0)		K' (mag)	R^b (mag)	$R-K'$ (mag)	FWHM ^c ($''$)
C16-ERO1	16:24:01.22	+55:38:49.0	$18.56^{+0.05}_{-0.06}$	$26.04^{+1.00}_{-1.00}$	7.48	2 $''$ 0
C16-ERO2	16:24:04.99	+55:38:26.2	$18.90^{+0.08}_{-0.09}$	$24.97^{+0.75}_{-0.44}$	6.07	1 $''$ 0
C16-ERO3	16:24:28.83	+55:43:10.4	$19.00^{+0.07}_{-0.07}$	$25.14^{+0.33}_{-0.26}$	6.14	0 $''$ 4
C16-ERO4	16:24:43.84	+55:49:40.6	$18.98^{+0.05}_{-0.06}$	$25.17^{+1.00}_{-1.00}$	6.19	1 $''$ 0
C16-ERO5	16:25:05.53	+55:39:54.4	$18.92^{+0.07}_{-0.06}$	$25.64^{+0.47}_{-0.33}$	6.72	1 $''$ 1
C16-ERO6	16:25:13.11	+55:48:30.4	$18.78^{+0.04}_{-0.05}$	$24.86^{+1.00}_{-0.53}$	6.08	0 $''$ 9
C16-LMS1	16:25:00.63	+55:44:44.3	$18.57^{+0.10}_{-0.10}$	$26.00^{+1.00}_{-1.00}$	7.43	0 $''$ 0
C16-LMS2	16:23:57.24	+55:46:27.5	$16.32^{+0.05}_{-0.05}$	$23.06^{+0.09}_{-0.09}$	6.74	0 $''$ 0

^aERO:Extremely Red Object; LMS:Low Mass Star (see section 3.2).

^bThe uncertainties on the R -band magnitudes of objects below the 2σ detection limit have been arbitrarily set to 1 $''$ 0. This represents taking a 2σ marginal detection to 5σ , where the object presumably would have been detected.

^cFWHM deconvolved from the seeing. The two low-mass stars are unresolved.

Table 2. Color Distributions

Magnitude Bin	Mean Color	FWHM
$16^{\text{m}}0 \leq K' < 17^{\text{m}}0$	3.24 ± 0.06	1.34 ± 0.10
$17^{\text{m}}0 \leq K' < 18^{\text{m}}0$	3.59 ± 0.05	1.86 ± 0.08
$18^{\text{m}}0 \leq K' < 19^{\text{m}}0$	3.73 ± 0.04	2.25 ± 0.06
$18^{\text{m}}5 \leq K' < 19^{\text{m}}5$	3.92 ± 0.04	2.60 ± 0.06
$19^{\text{m}}0 \leq K' < 20^{\text{m}}0$	3.93 ± 0.03	2.60 ± 0.04

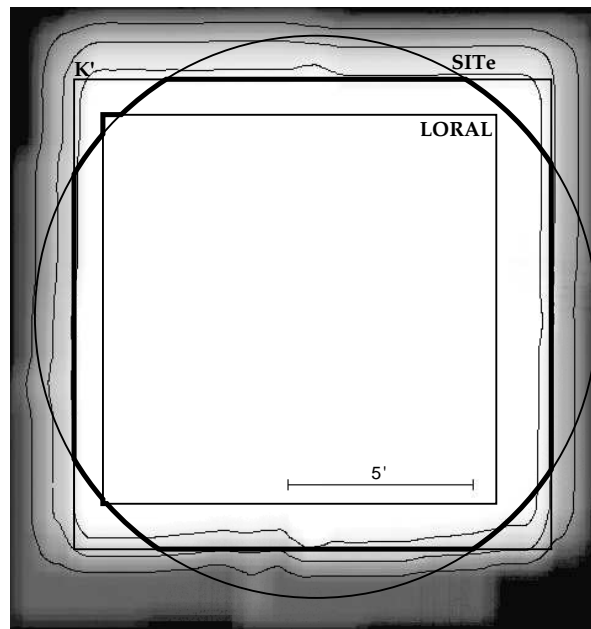


Fig. 1.— The grayscale background image shows the relative exposure time in the full K' mosaic. Three contours, at 1000, 3000, and 6000 seconds exposure time, are also plotted. The area used for the ERO survey is indicated (heavy line), showing the area of overlap between the K' image (outer square) and the two R images (LORAL (inner square) and SITE (circle) CCDs).

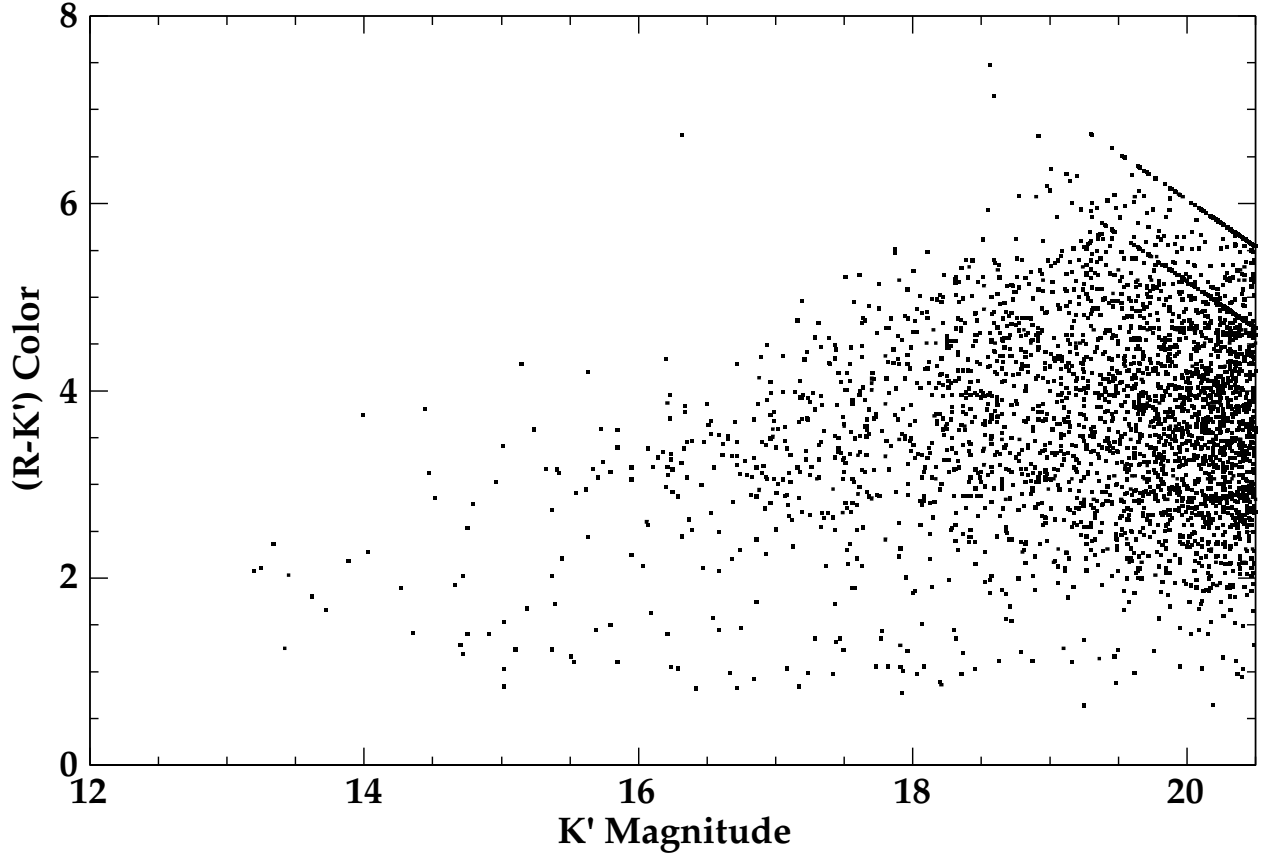


Fig. 2.— The R - K' color-magnitude diagram for the entire CADIS 16 h field. Two loci of points on diagonal lines are visible in the upper right corner. These loci are artifacts resulting from the use of different sized R images (see section 2.2 and Figure 1). The deeper limit represents the effective 2σ limit of $26^{\text{m}}04$ reached in the combined R images, while the brighter limit corresponds to the 2σ limit of $25^{\text{m}}17$ in the R image taken with the SITE CCD but outside of the area covered by the LORAL CCD. Objects which are undetected in the R data are plotted at the 2σ limit. The majority of objects with R - $K' < 2$ are stars.

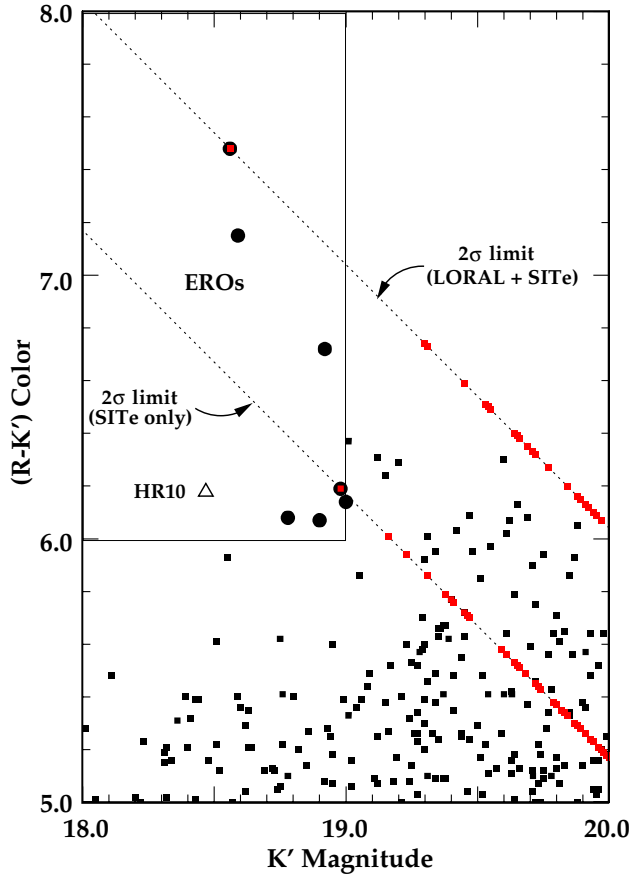


Fig. 3.— Enlarged portion of Figure 2 covering the area near the ERO selection region. Seven of the 8 bright EROs are marked with the large filled circles, the last ERO is off the plot to the left (at $K' = 16^m3$). The remaining objects from the 16^h field are plotted as filled squares. Objects which fall on the two diagonal lines are undetected in the R data at the 2σ level (see Figure 2 caption for details) and should be considered lower limits to the actual color. The location of HR 10 (open triangle) is shown for comparison. No published R -band magnitude for HR10 exists. We estimate the R magnitude to be $R \sim 25^m0$, derived from a linear interpolation between the B and I band fluxes for HR10 from Graham & Dey (1996).

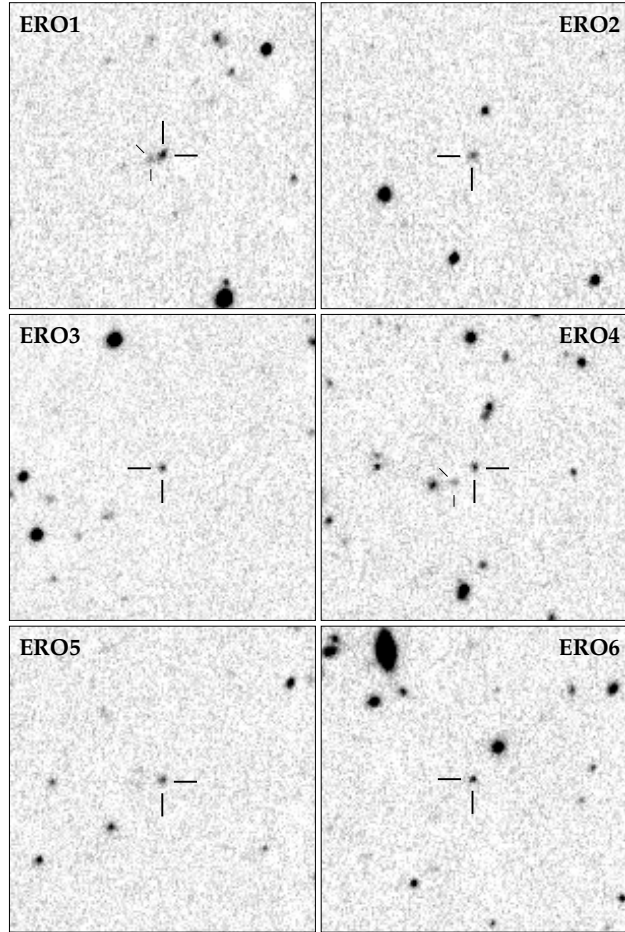


Fig. 4.— Finding charts for the 6 bright EROs. Each subimage is $60''$ square, with north up and east to the left. Both ERO1 and ERO4 have red companion galaxies to the southeast, indicated with the smaller tick marks.

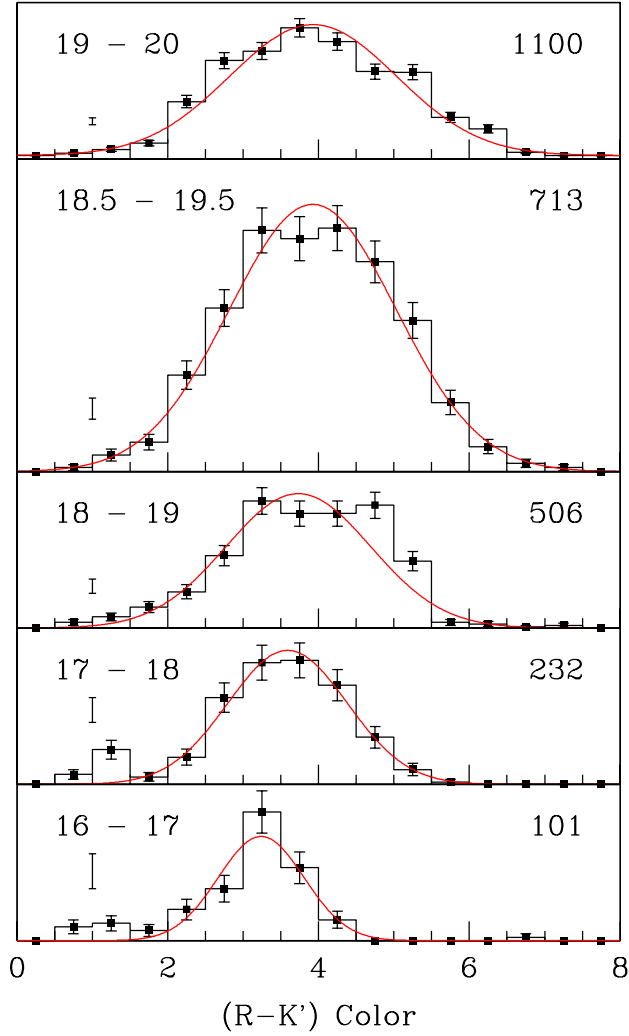


Fig. 5.— Color histograms for different magnitude bins in the 16 h field data. Magnitude ranges are indicated in the upper left corner of each graph, the total number of objects used for each subpanel in the upper right corner. The histograms show the actual data, with poisson uncertainties indicated. Mean color and FWHM for the Gaussian fits are given in Table 2. The vertical scale bars at color = 1.0 in each subpanel are 10 units high.